

Schrödinger/Luttinger Approach to Scaled MOS Transport for Various Crystal Orientations and its Experimental Verifications

Takako Okada and Hisao Yoshimura*

Corporate Research & Development Center, Toshiba Corporation, Kawasaki 212-8582, Japan

*System LSI Division, Semiconductor Company, Toshiba Corporation, Yokohama, Japan

e-mail: t-okada@amc.toshiba.co.jp

INTRODUCTION

In scaled device designing for the 40 nm regime and beyond, deeper physical insight into channel transport will be required than previously. A Schrödinger/Luttinger approach to scaled MOS transport was applied for the first time to various crystal orientations, channel directions, applied voltages and mechanical stresses together with experimental verifications. Typical findings obtained in this work are as follows: (1)marked variations of inversion carrier distributions have been calculated among (110), (111), (112), (120) and (100) surfaces, (2)significant differences in channel conductivities of p-channel MOS have been simulated between triode and pentode regions, and (3)effective mass characteristics have been output as functions of germanium concentration.

SCHRÖDINGER/LUTTINGER BASED APPROACHES

Newly developed Schrödinger/Luttinger prototype codes are composed of (1)extended Luttinger^{[1][2][3]} equations with stress/strain tensor and matrix solvers, (2)Poisson solver^[4], and (3)Monte Carlo parts^[5] with anisotropic subband energy and scattering rates linked with each other as shown in Figs.1 and 2. Typical subband structures for p-channel inversion layers, band diagrams of (110) Si and inversion charge distribution are presented in Figs.3, 4 and 5, respectively. It should be noted that distinctive variations of hole inversion band scheme were calculated for the first time among (110), (111), (120), and (100) surfaces in terms of external stress, and significant differences in channel carriers of p-channel MOS have been simulated among Si/SiGe and Ge substrates. Figure 6 shows energy dependence of scattering rate results for carrier transports. Real-time snapshots of carrier distributions and drift mobility are demonstrated in Figs.7, 8 and 9. From the above results, it is first clarified quantitatively that (1)stress sensitivities of effective masses in Si/Ge and Ge substrate have been simulated and (2)the mobility advantage of [110] hole carriers on strained

(100)Si is simulated to be smeared in high electric field. In order to verify the modes and simulated results, MOS cantilever experiment have been conducted as shown in Fig.10. Drain currents were measured upon application of external uniaxial stress. The amounts of additional strain $\Delta\varepsilon_{ij}$ were calculated by means of the following equation:

$$\Delta\varepsilon_{ij} = (3Z \times b \times \Delta h) / L^3,$$

where Δh , Z and L are indicated in Fig.10 and b is a half of the wafer thickness. Δh was measured using a micrometer head. In the case of [110] Si p-channel on (100) Si, measurement reveals that drain current gain decreases with compressive strain $\Delta\varepsilon_{ij}$ in the pentode region contrarily to the triode region, which is consistent with the results in Fig3.

SUMMARY

A Schrödinger/Luttinger approach to scaled MOS transport was applied for the first time to various kinds of crystal orientations, channel directions, applied voltages and mechanical stress together with experimental verifications. Through intensive analysis, it has been determined that Si/Ge and Ge are promising materials from the view-point of scaled CMOS drivability in conjunction with mechanical stress and crystal orientations. Details of mathematical derivations in Schrödinger/Luttinger part and scattering rate procedures will also be reported with calling upon current references^{[6][7]} at the IWCE conference.

REFERENCES

- [1] J. M. Luttinger and W. Kohn, Phys. Rev. **97**, 869 (1955).
- [2] S. Rodriguez, J. A. Lopez-Villanueva, I. Melchor and J. E. Carceller, J. Appl. Phys. **86**, 438 (1999).
- [3] D. A. Broido and L. J. Sham, Phys. Rev.B. **31**, 31888 (1985).
- [4] F. Stern, J. Computational Phys. **6**, 56 (1970).
- [5] J.E.Dijkstra and W. Th. Wenckebech, J. Appl. Phys. **81**, 259 (1997).
- [6] M. V. Fischetti and S. E. Laux, Phys. Rev.B **48**, 2244 (1993).
- [7] M. V. Fischetti et al., J. Appl. Phys. **92**, 7320 (2002).

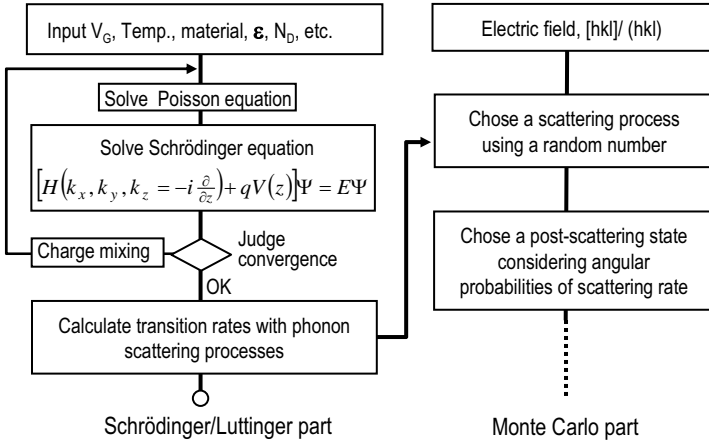


Fig.1 Block diagram and flows of our newly developed Schrödinger/Luttinger based codes.

$$H = \begin{pmatrix} P+Q & S & R & 0 & -iS/\sqrt{2} & i\sqrt{2}R \\ S^* & P-Q & 0 & R & i\sqrt{2}Q & -i\sqrt{3}/2S \\ R^* & 0 & P-Q & -S & i\sqrt{3}/2S^* & i\sqrt{2}Q \\ 0 & R^* & -S^* & P+Q & i\sqrt{2}R^* & iS^*/\sqrt{2} \\ iS^*/\sqrt{2} & -i\sqrt{2}Q^* & -i\sqrt{3}/2S & -i\sqrt{2}R & P-\Delta & 0 \\ -i\sqrt{2}R^* & i\sqrt{3}/2S^* & -i\sqrt{2}Q^* & -iS/\sqrt{2} & 0 & P-\Delta \end{pmatrix}$$

$$P = -\frac{\hbar^2}{2m_0} \gamma_1 (k_x^2 + k_y^2 + k_z^2) + a(\varepsilon_{xx} + \varepsilon_{yy} + \varepsilon_{zz})$$

$$Q = \frac{\hbar^2}{2m_0} \left\{ \left(\frac{\gamma_2}{2} - \frac{3\gamma_3}{2} \right) k_x^2 - \gamma_2 k_y^2 + \left(\frac{\gamma_2}{2} + \frac{3\gamma_3}{2} \right) k_z^2 \right\} + \left(-\frac{b}{4} \right) (\varepsilon_{xx} + \varepsilon_{yy}) + \left(\frac{b}{2} \right) \varepsilon_{zz} - \frac{\sqrt{3}}{2} d \varepsilon_{xy}$$

$$R = \frac{\hbar^2}{2m_0} \left(-\frac{\sqrt{3}}{2} \gamma_2 \right) (k_x^2 - 2k_y^2 + k_z^2) + \frac{\hbar^2}{2m_0} \left(-\frac{\sqrt{3}}{2} \gamma_3 \right) (k_x^2 - k_z^2) + \frac{\hbar^2}{2m_0} (-i2\sqrt{3}\gamma_3) k_x k_y + \frac{\sqrt{3}}{4} b (\varepsilon_{xx} + \varepsilon_{yy} - 2\varepsilon_{zz}) - d \left\{ \frac{1}{2} \varepsilon_{xy} + \frac{i}{\sqrt{2}} (\varepsilon_{xz} - \varepsilon_{yz}) \right\}$$

$$S = \frac{\hbar^2}{2m_0} i \left(-2\sqrt{3} \right) \gamma_2 \left(k_x + i \frac{\gamma_3}{\gamma_2} k_y \right) k_z + i \frac{\sqrt{3}}{2} b (-\varepsilon_{xx} + \varepsilon_{yy}) - \frac{d}{\sqrt{2}} (\varepsilon_{xz} + \varepsilon_{yz})$$

Fig.2 Outline of typical 6×6 Luttinger Hamiltonian for Si(110). Some of notation here are consulted on Ref [2].

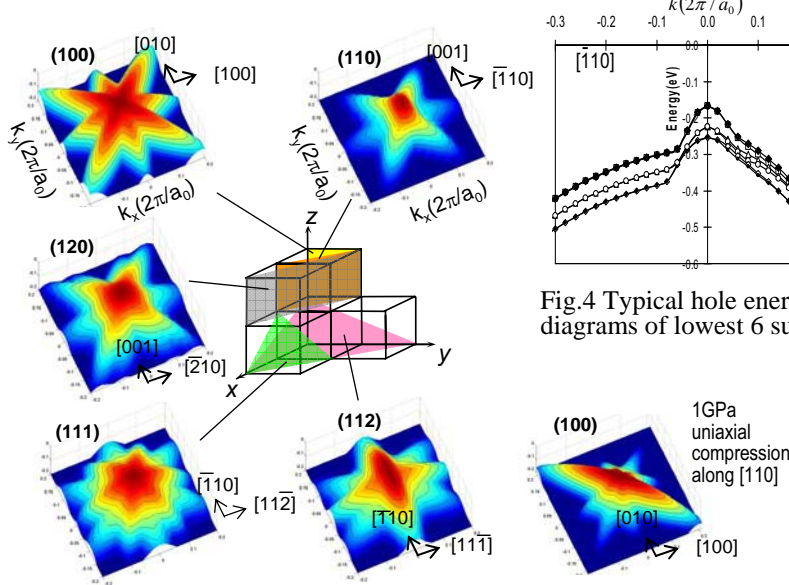


Fig.3 Typical perspective plot of hole lowest subbands of Si in terms of surface orientation. Interval of contours is 20meV.

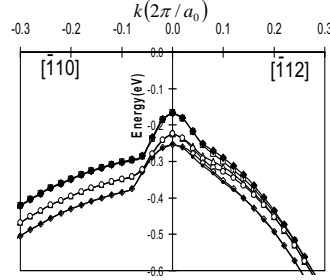


Fig.4 Typical hole energy diagrams of lowest 6 subbands.

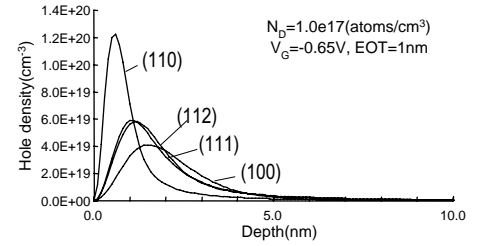


Fig.5 In-depth profiles of carrier density.

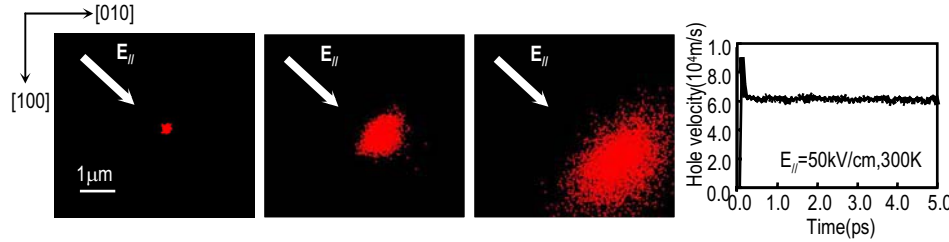


Fig.7 Typical snapshots of hole distribution in electric field. Lateral electric field $E_{||}$ is 50kV/cm.

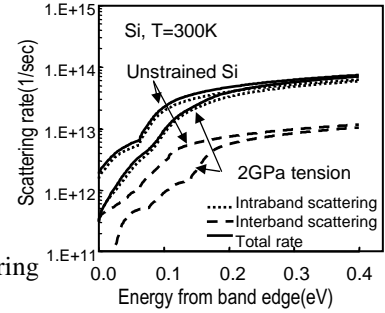


Fig.6 Scattering rate.

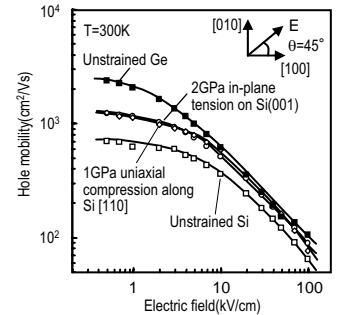


Fig.8 Hole mobility as a function of the lateral electric field.

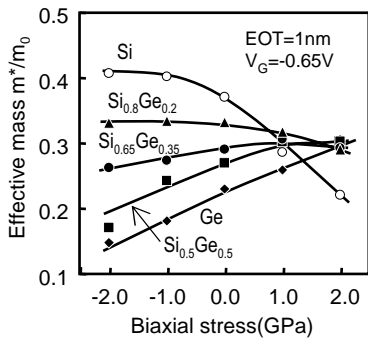


Fig.9 Hole effective mass of lowest subband in Ge and $Si_{1-x}Ge_x$ as a function of biaxial stress and material composition.

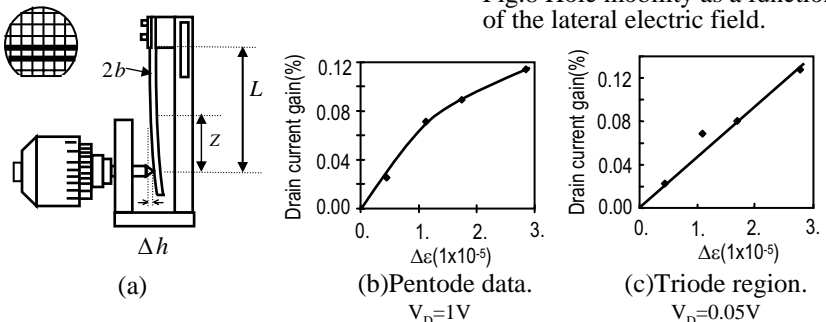


Fig.10 MOS cantilever experimental setup(a) and experimental results(b)(c). Dimensions of the specimen are as followed; $L=39.08\text{mm}$, $Z=9.60\text{mm}$ and $2b=0.70\text{mm}$. S/D is located on transversal to the beam, and generated strain is compressive on the S/D direction.